# Laser-Enabled Carbon Dot Coating for Powder Bed Fusion Metal Parts

Paper #: 0945_1413_000147

Mohammad Mohammadzadeh Sanandaji[1], Benjamin Nelson[1], Mohammad Ikram Haider[1], Hongtao Ding[1]*

[1]Department of Mechanical Engineering, University of Iowa, Iowa City, IA 52242, USA
*Corresponding author. Tel.: +1 3193355674; E-mail: hongtao-ding@uiowa.edu

## Abstract

The development of environmentally friendly surface engineering techniques for 3D-printed metal parts is crucial for fluid-related applications. This study introduces two innovative, PFAS-free methods to achieve superhydrophilic surfaces on laser powder bed fusion (L-PBF) fabricated AlSi10Mg and Ti6Al4V samples. The first method involves the direct application of gel-like carbon dots (G-CDs) coating inducing superhydrophilicity. The second method integrates nanosecond laser texturing to create microgrooves that facilitate capillary-driven liquid transport, followed by G-CDs coating, resulting in a stable superwicking surface. This laser-based method also offers precise control over fluid direction by adjusting the orientation of the microgrooves, allowing the surface to be designed with programmable wicking paths. Both methods maintain a water contact angle below 10° for over 30 days. Surface features, surface chemistry, wettability, wicking behavior are measured on AlSi10Mg and Ti6Al4V samples through Scanning Electron Microscopy (SEM), Electron Dispersive Spectroscopy (EDS), contact angle goniometer, and high-speed camera, respectively.

## Keywords

Laser powder bed fusion; Superhydrophilic surface; Organic coating; Carbon dots.

## 1. Introduction

In recent years, additive manufacturing (AM) technologies, particularly laser powder bed fusion (L-PBF), have gained significant attention for their ability to fabricate complex metal parts with intricate geometries [1,2]. The development of 3D-printed metal components, including aluminum and titanium alloys, has opened new possibilities in fields such as bioengineering [3], catalysis [4], microfluidics, heat exchanger design [5,6]and thermal process engineering [7]. However, the surface wettability of L-PBFed metal parts often presents challenges. These surfaces typically exhibit high surface energy, resulting in hydrophilic properties, which are prone to instability over time. When exposed to air, the wettability of these parts can change, leading to a transition from hydrophilic to hydrophobic states, often reducing their performance in practical applications[8–10]. To resolve this issue, this study aims to develop a surface treatment strategy to achieve a durable superwicking effect by precisely tailoring both surface topography and surface chemistry.

Surface wettability is typically evaluated based on the water contact angle (θw), which describes the interaction between a liquid and a solid surface. A surface is classified as superhydrophobic when θw is greater than 150°, hydrophobic when it falls between 90° and 150°. Conversely, surfaces with θw below 10° are considered superhydrophilic, while hydrophilic surfaces have values between 10° and 90° [11]. For instance, research by Sun et al. [12] found that untreated 316L stainless steel exhibited slight hydrophobicity (θw ~96°). However, introducing an inverted trapezoidal structure significantly enhanced hydrophilicity, achieving θw values below 10°. Similarly, Neukaufer et al. [13] observed that θw for raw 316L stainless steel varied between 70° and 92°, depending on the printing orientation. When 316L stainless steel was processed via laser powder bed fusion (L-PBF) to incorporate square pillars and rectangular channels, θw measurements ranged from 80° to 100°. In the case of aluminum alloys, L-PBF-fabricated AlSi10Mg parts exhibited slight hydrophilicity with θw around 70° [14]. Likewise, Ti6Al4V components in their as-built state displayed θw values close to 70° [15], with other studies reporting variations between 75° and 105°, influenced by alloy composition and processing conditions. These differences in wettability across studies can be attributed to factors such as laser processing parameters, post-treatment methods, cleaning procedures, and exposure to environmental conditions.

Various post-processing strategies have been investigated to enhance the hydrophilicity of L-PBF-processed metal alloys. One study explored electrochemical anodization's impact on Ti6Al4V wettability, revealing a reduction in θw from 68° to 11° [16]. This alteration also promoted better protein absorption and cell adhesion, making it advantageous for biomedical applications. Notably, while anodization significantly modified wettability, it did not considerably change the surface roughness. Similarly, acid etching has been used to alter the surface characteristics of L-PBF-fabricated TA6V titanium alloy [17]. Immersion in a 3% HF/10% HNO3 acid solution for 15 minutes led to a decrease in θw from 75° to 48°, demonstrating the effectiveness of chemical treatments in modifying surface wettability. However, while these approaches improve hydrophilicity, they have yet to achieve superwicking behaviour.

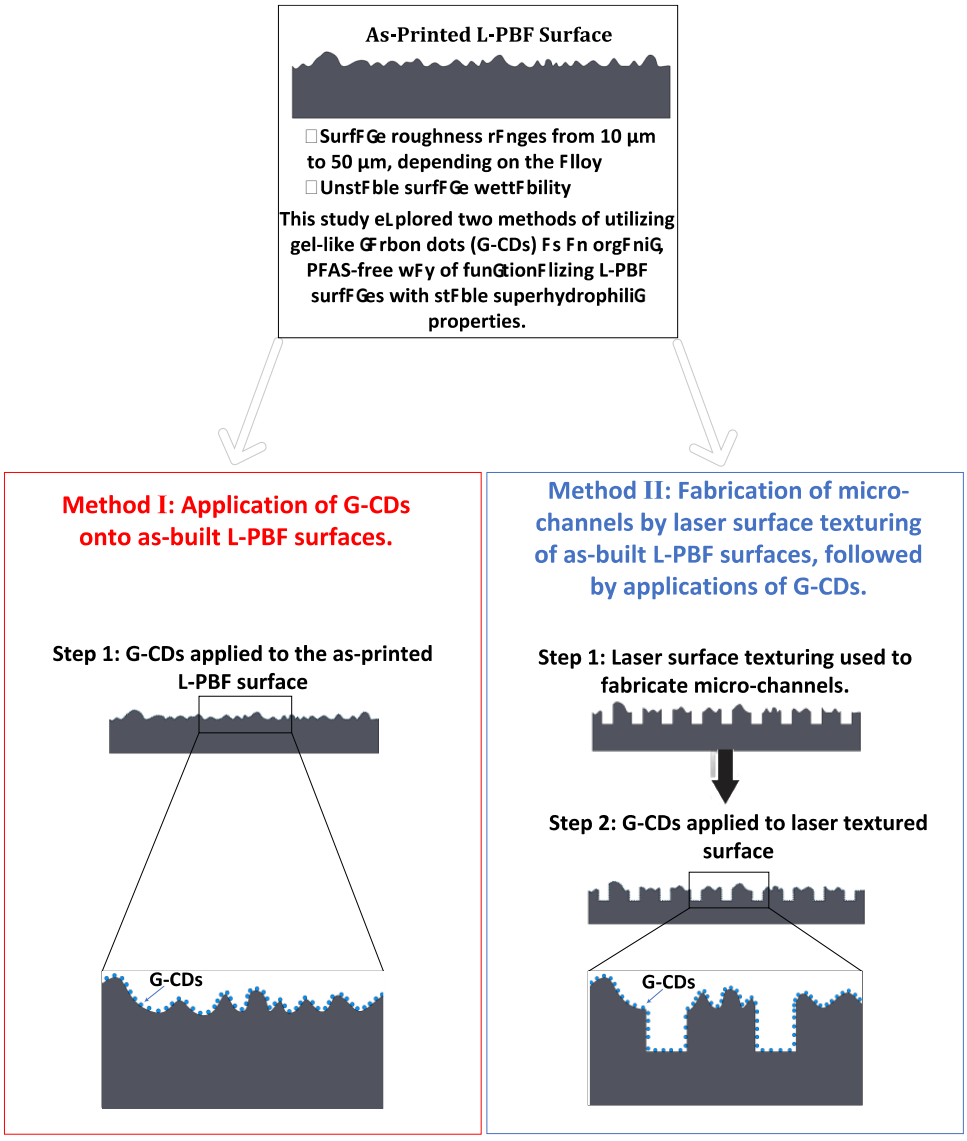


Fig. 1. Proposed superhydrophilic surface processing methods for metal 3d printed parts.

This research introduces two innovative and ecofriendly approaches to achieve superhydrophilic properties on L-PBFed metal samples, aimed at enhancing fluid transport and thermal management applications. As

illustrated in Fig. 1, Method I focuses on the direct application of a novel organic, PFAS-free coating which is gel-like carbon dots (G-CDs) to the metal surface without actively modifying the as-built (L-PBF) topography. While, in Method II, the combination of nanosecond laser surface texturing and G-CDs coating allows for the creation of microscale and nanoscale topographies on the metal surface, enhancing surface roughness and increasing wettability.

## 2. Experiments

In this study, AlSi10Mg and Ti6Al4V were selected as the materials of interest due to their widespread adoption in AM. These alloys are extensively utilized in engineering applications due to their wettability [18], making them ideal candidates for investigating surface characteristics and wettability modifications. Laser Powder Bed Fusion (L-PBF) was employed for sample fabrication, given its cost efficiency and high process repeatability. The specimens were manufactured at the Quad City Manufacturing Lab using an EOS M270 system. All LPBF samples were fabricated using optimized process parameters to ensure metallurgically sound parts with >99.9% relative density, minimizing internal defects and ensuring consistent surface integrity for coating and wettability analysis.

To examine the effect of build orientation on surface properties, two distinct orientations were implemented, the first orientation (denoted as //) corresponds to a 60° inclination relative to the build plane, while the second (denoted as =) represents a 0° inclination. These orientations were selected to analyze variations in surface morphology and wettability.

Each layer was processed using two primary laser scanning strategies: (1) striping scans and (2) contouring scans. The striping scan technique was used to fuse the bulk material; however, it introduced surface irregularities at the transition points where the laser scan started and stopped. To address this issue, additional contouring scans were applied along the outer edges of the 0° test surfaces, which exposed the cross-sections of the printed layers. This additional processing step was implemented to minimize defects associated with striping scan transitions, leading to improved surface uniformity. A comprehensive summary of the L-PBF process parameters, including the continuous wave (CW) fiber laser settings, is provided in Table 1.

### *Method I: Gel-like Carbon Dots Coating*

Method I was designed to modify the surface chemistry of L-PBF-fabricated parts while preserving their original topography. Prior to applying the G-CDs, the as-built parts were thoroughly cleaned in 3 step process: 3 minutes ultrasonic cleaning in acetone, followed by 3 minutes ultrasonic cleaning ethyl alcohol, followed by 3 minutes ultrasonic cleaning in distilled water. The gel-like carbon dots (G-CDs) used for coating were synthesized at 140 °C, yielding nanoparticles with diameters ranging from 2 to 10 nm. These nanoparticles contain carboxyl (-COOH) and hydroxyl (-OH) functional groups, which promote dispersion stability in water and improve chemical durability [19]

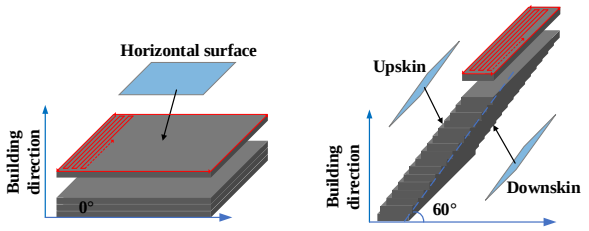


Fig. 2. Design of L-PBF experiments in this study with two different building orientations

Two aqueous G-CDs solutions 1 wt% and 2 wt% were prepared to enhance and sustain surface wettability. As illustrated in Fig. 3c, the coating was applied manually using a spray method. A laboratory syringe fitted with a blunt-tip needle was used to dispense the G-CDs solution, ensuring precise and uniform coverage. Approximately 0.1 mL of solution was applied to each 13 mm × 13 mm sample to ensure full surface infiltration. After application, the specimens were left to rest for two hours and then dried using compressed air at room temperature.

In addition to improving surface energy, this organic coating acts as a protective barrier, preventing contamination-induced degradation of wettability over time. Previous studies have reported that G-CDs coated surfaces maintain superhydrophilicity for more than 30 days [20]. The nanoparticles also exhibit strong ultraviolet (UV) absorption at ~270 nm and fluorescence emission around 450 nm[21]. Furthermore, the abundance of carboxyl groups contributes to a negatively charged surface, further enhancing their interaction with the substrate.

Notably, the G-CDs coating used in this study is colorless and nearly invisible to the naked eye. When applied to the metal surface, it does not alter the visual appearance, gloss, or surface finish of the samples. This transparency is especially important for applications where maintaining the original aesthetic, texture, or identification markings of the component is critical. Unlike many surface coatings that impart a visible film,

Table 1. L-PBF operational parameters for the AlSi10Mg and Ti6Al4V parts

| Surface | CW laser power $P$ (W) | Scan speed $V$ (mm/s) | Powder size $d_p$ (µm) | Hatch distance $h$ (mm) | Layer thickness $t$ (mm) | Energy density $E_d$ ($E_d = \frac{P}{Vht}$) (J/mm³) |
|---|---|---|---|---|---|---|
| AlSi10Mg= | 193.6 | 800 | 20-63 | 0.2 | 0.03 | 40.3 |
| AlSi10Mg// | 150 | 1250 | 20-63 | 0.2 | 0.03 | 20 |
| Ti6Al4V= | 170 | 1250 | 15-45 | 0.1 | 0.03 | 45.3 |
| Ti6Al4V// | 150 | 1250 | 15-45 | 0.1 | 0.03 | 40 |

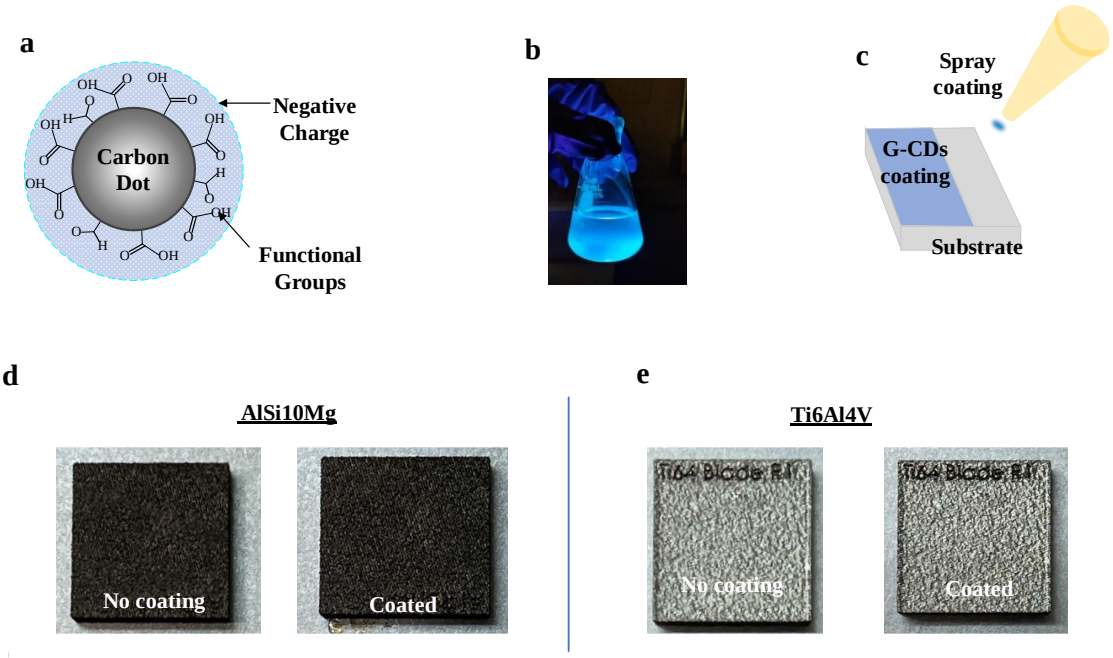


Fig. 3. Overview of Method I: G-CDs-based organic coating: (a) Molecular structure of gel-like carbon dots [22]; (b) Prepared G-CDs solution under UV[23]; (c) schematic of the coating process; (d) comparison between uncoated and coated AlSi10Mg samples (e) comparison between uncoated and coated Ti6Al4V samples.

discoloration, or haze, the G-CDs layer offers a visually neutral modification, making it suitable for use in devices requiring optical clarity, such as biomedical tools, aerospace components, or consumer products where surface branding or color coding must remain intact.

### *Method II: Combining laser texturing and G-CDs coating*

In method II, both surface topography and surface chemistry were engineered. This approach consisted of two sequential steps: (1) nanosecond laser texturing in ambient air, followed by (2) surface modification using G-CDs.

In the first step, a nanosecond pulsed laser was utilized to fabricate unidirectional microchannels. The formation of parallel microchannels facilitated capillary-driven liquid flow, enabling rapid and

sustained wicking. Additionally, melt expulsion during laser processing generated nanostructures that increased surface roughness and permeability both essential for maintaining superwicking behavior. This laser-induced texture also provided an ideal foundation for the subsequent application of G-CDs.

To fabricate fine microgrooves, a Nd:YAG nanosecond laser (Spectra-Physics Quanta-Ray Lab-150, 1064 nm) was operated at a pulse repetition rate of 10 Hz, an average power of 0.9 W, and a pulse duration of 100 ns under ambient conditions. The laser beam was precisely guided onto the sample surface using a galvanometer scanner (SCANLAB intelliSCAN 20) equipped with an f-theta lens (255 mm focal length), ensuring a uniform energy distribution across the substrate, as illustrated in Fig. 4a.

The laser scanning speed was set at 1.2 mm/s, with a spot size of 100 µm, producing well-defined and consistent microchannels as shown in Fig.3b. The process was conducted in ambient air, facilitating in-situ oxidation of the aluminum and titanium surfaces, which contributed to modifications in surface energy. To achieve uniform texturing, a fast-scanning strategy was employed with a 50% overlap between successive laser pulses. This strategy was optimized to maximize surface roughness while maintaining the structural integrity of the samples. Following laser texturing, the samples underwent the same G-CDs treatment as described in Method I. The application of G-CDs on the laser-treated surfaces was expected to further enhance wettability, improve wicking behavior, and provide long-term surface stability. The synergistic effects of laser-induced surface structuring and chemical functionalization were investigated to assess their impact on hydrophilicity and liquid transport behavior.

Notably, the laser texturing approach provides precise control over the orientation and layout of the microgrooves, enabling us to guide fluid movement along predetermined paths as shown in Fig. 4d. By simply adjusting the scanning direction and pattern during laser processing, it becomes possible to design surfaces that promote directional wicking and targeted liquid spreading. This level of control is especially useful for creating smart surfaces where the transport of fluids can be tailored to specific applications.

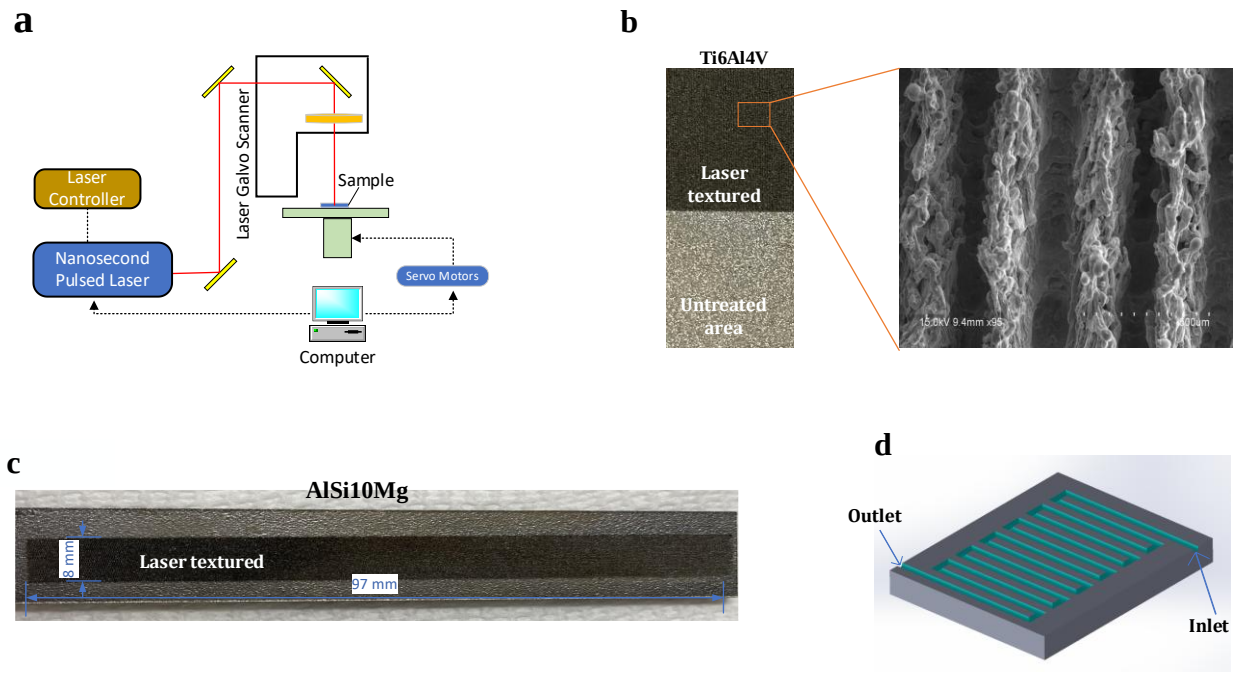


Fig. 4. Laser surface processing and topography. (a) experimental setup of nanosecond laser texturing; (b) laser treated Ti6Al4V (=) sample, with SEM micrograph for microgrooves; (c) laser treated AlSi10M sample with a wicking path; (d) a general design of surface wicking pattern.

The wettability of the samples was evaluated through static contact angle measurements. A contact angle goniometer (Rame-Hart Model 100), equipped with a high-resolution CMOS camera (6–60× magnification, Thor Laboratories), was employed to determine the static water contact angle. To analyze fluid transport

behavior on laser-textured and G-CDs-coated surfaces, high-speed imaging was utilized, enabling precise assessment of liquid spreading dynamics, wicking height, and transport velocity. Additionally, the morphology and chemistry of the superwicking surfaces was examined via Scanning Electron Microscopy (SEM) using a Hitachi S-4800 equipped with a Bruker Energy-Dispersive Spectroscopy (EDS) system.

## 3. Results and Discussion

### *3.1 Surface Texture*

The surface topographic characteristics of the as-built parts were analyzed using confocal microscopy. Fig. 5. presents the surface contour plots for the 0° and 60° downskin surfaces of Ti6Al4V and AlSi10Mg samples. The surface roughness of the Ti6Al4V samples is significantly lower than that of the AlSi10Mg samples, and the surface morphology of Ti6Al4V appears much more refined. This difference in surface morphology reflects inherent variations in the laser powder bed fusion (LPBF) process response between the two alloys. Ti6Al4V tends to solidify with more uniform thermal gradients and cooling rates, leading to finer surface features, while AlSi10Mg often exhibits more pronounced balling, satellite formation, and partially melted powder particles, which contribute to a rougher surface [24] [25]

Such morphological differences are critical, especially for applications involving surface coatings or wettability modification. A smoother and more uniform base surface, like that of Ti6Al4V, may facilitate more controlled chemical functionalization or coating adherence, but it can also limit surface-driven enhancements such as capillary wicking or droplet spreading that benefit from micro- and nanoscale roughness. Conversely, the rougher AlSi10Mg surfaces inherently provide a larger effective surface area, which can amplify surface interactions but may also introduce variability[26]

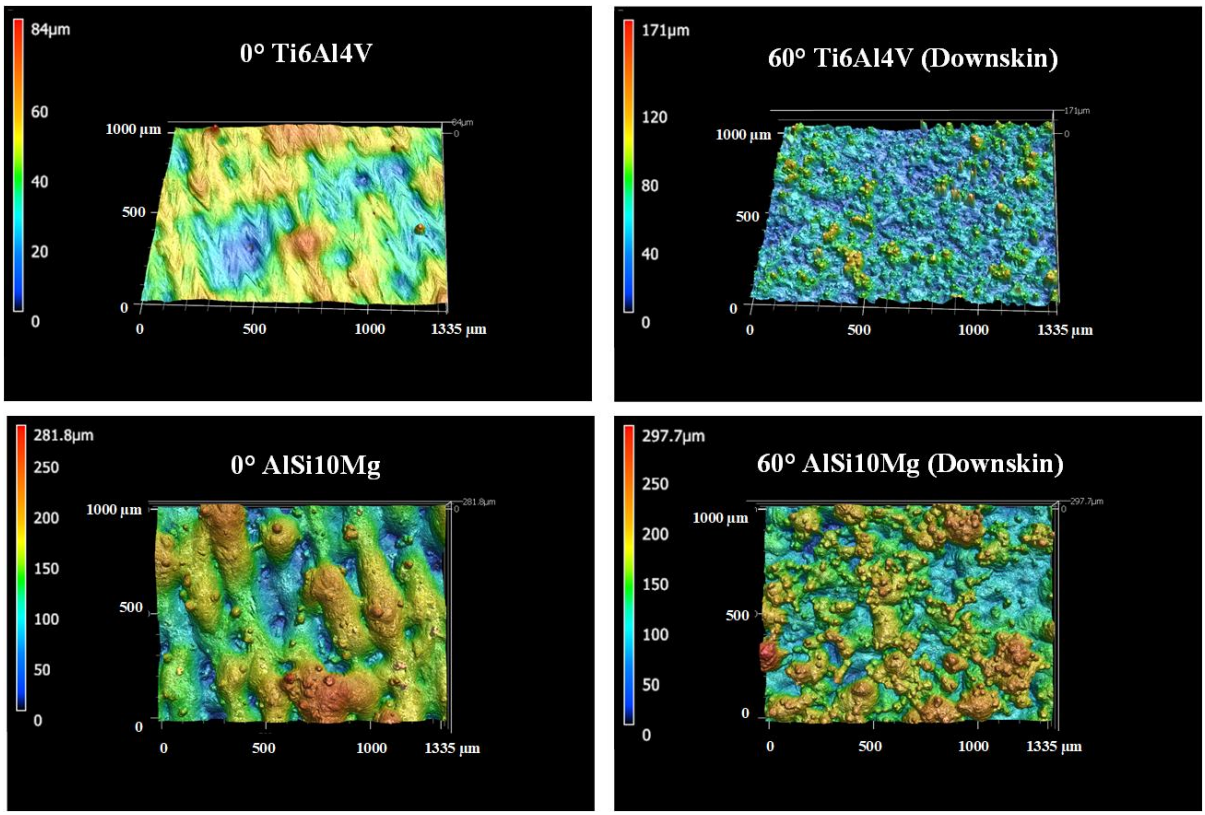


Fig. 5. Surface morphology of the as-fabricated parts using confocal microscopy.

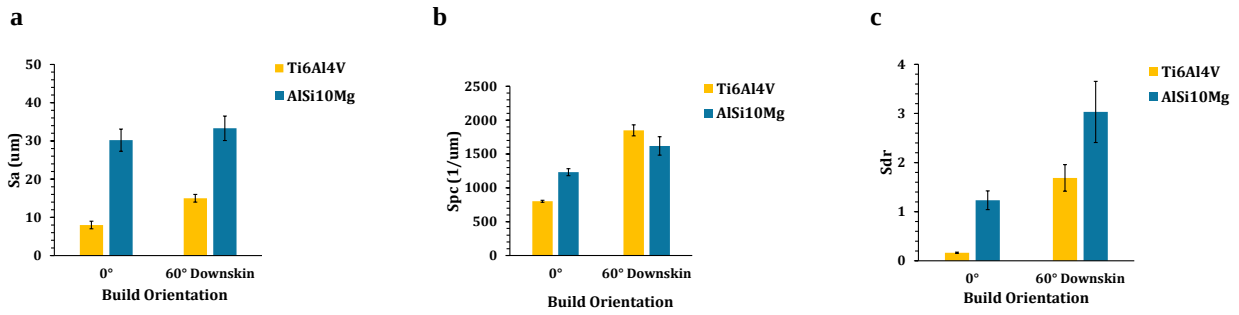


Fig. 6. Plots of the surface roughness parameters: (a) average surface roughness (Sa); (b) arithmetic mean curvature (Spc); (c) developed surface area ratio (Sdr) for the 0° and 60° downksin surfaces of Ti6Al4V and AlSi10Mg samples.

A detailed comparison of surface roughness parameters namely the average surface roughness (Sa), arithmetic mean curvature (Spc), and developed surface area ratio (Sdr) is presented in Fig. 6. The Sa values confirm that Ti6Al4V surfaces exhibit significantly smoother profiles than AlSi10Mg surfaces. The Spc parameter, which characterizes the sharpness and refinement of surface features, is typically higher for surfaces with finer topographical details. As shown in Fig. 6, the 60° Ti6Al4V surface is composed of smaller, more refined features compared to its AlSi10Mg counterpart, while the 0° Ti6Al4V surface appears notably flatter and smoother than the 0° AlSi10Mg surface.

The Sdr value, defined as the ratio of the actual surface area to the projected surface area, offers insight into the degree of surface development. Higher Sdr values observed in the AlSi10Mg samples indicate a more textured and developed surface, resulting in a greater effective surface area.

These distinctions in surface morphology help to explain the wettability behavior observed in Fig. 9. On as-printed surfaces (Method I), the G-CDs coating more effectively reduces the water contact angle on AlSi10Mg compared to Ti6Al4V, likely due to the higher inherent surface roughness of AlSi10Mg. However, when Ti6Al4V surfaces are micro-textured using additive nanosecond laser texturing (aNLT) to form microchannels (Method II), the increased roughness and surface area significantly enhance the performance of the G-CDs coating in lowering the contact angle.

### *3.2 Surface Chemistry*

To quantitatively evaluate the presence of surface functional groups, the elemental composition of L-PBFed AlSi10Mg samples coated with G-CDs was examined using EDS analysis. While data for aluminum, silicon, magnesium, carbon, and oxygen were collected, only the elemental maps for aluminum, carbon, and oxygen are discussed here for clarity. As shown in Fig. 7, aluminum used as a reference element appears consistently distributed across the surface. In contrast, the presence of carbon and oxygen in the elemental maps is primarily attributed to the surface functional groups introduced by the G-CDs coating. These gel-like carbon dots are rich in carboxyl (-COOH) and hydroxyl (-OH) groups, which are known to enhance water affinity and significantly improve surface wettability. The detected carbon originates from the carbon backbone of the dots, while the oxygen signal reflects the abundance of oxygen containing functional groups anchored to their surfaces. These functional groups play a critical role in modifying surface chemistry by increasing surface polarity and enabling strong hydrogen bonding with water molecules. As the concentration of G-CDs increases, more carboxyl and hydroxyl groups are deposited on the surface, which corresponds to the higher oxygen content observed in the EDS maps. Therefore, the distribution of carbon and oxygen not only confirms the successful application of the G-CDs coating but also provides evidence of effective chemical functionalization an essential factor for achieving and sustaining superhydrophilic behavior on the treated surfaces.

In addition, Fig. 8 shows bar charts that compare the percent compositions of carbon, oxygen, and aluminum reported by the EDS quantitative analysis. The charts in the figure compare the quantitative results for similar surfaces treated by the 1% and 2% G-CDs solutions, with the chart of the left focusing on Method I and the chart on the right focusing on Method II. Comparing similar surfaces treated by the 1% and 2% G-CDs solutions using Method I or Method II – the surfaces

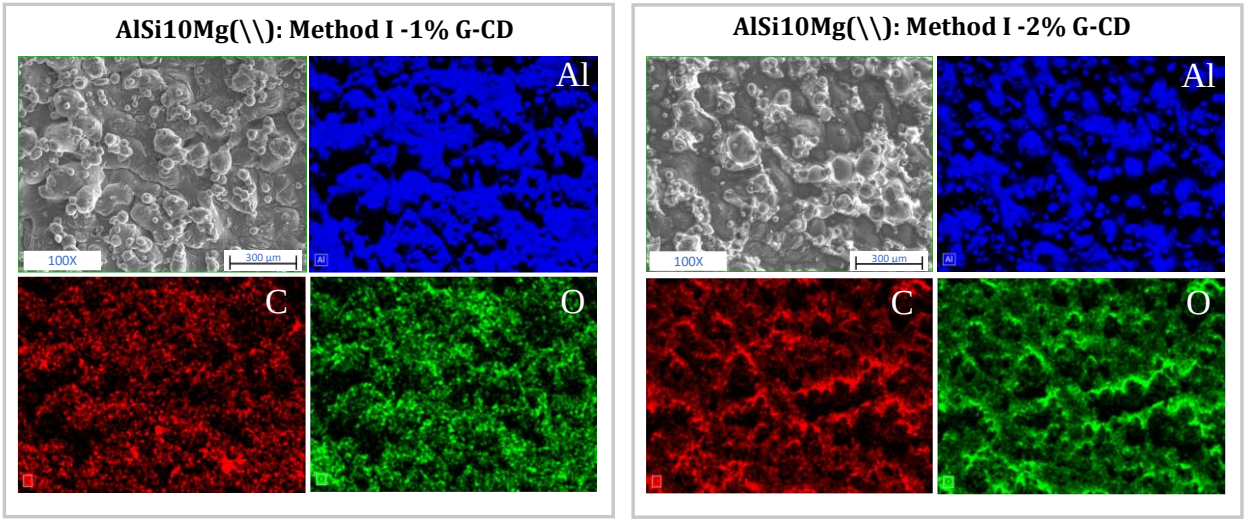


Fig 7. EDS elemental distribution maps for AlSi10Mg (\\) samples treated with 1% and 2% G-CDs concentrations using Methods I.

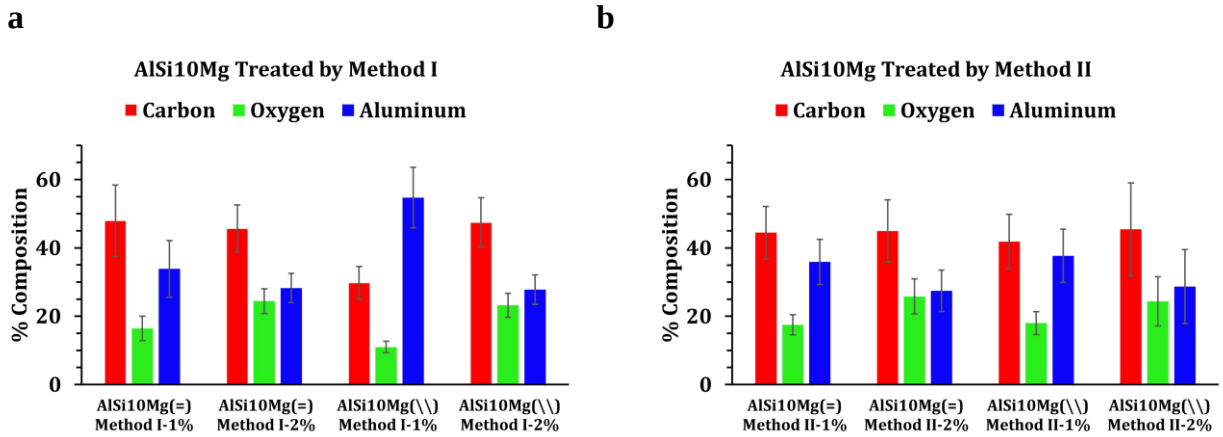


Fig. 8. Bar charts comparing percent composition of carbon, oxygen, and aluminum reported by the EDS quantitative analysis: (a) Results of 1% and 2% G-CDs solutions used with Method I; (b) Results of 1% and 2% G-CDs solutions used with Method II.

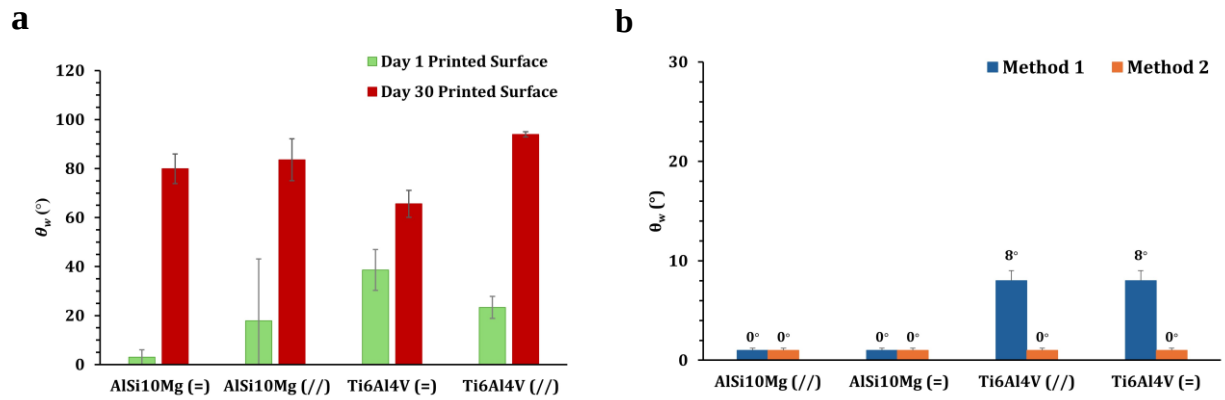


Fig. 9. Surface Wettability: (a) surface wettability of L-PBF samples over time; (b) stability of surface wettability for L-PBF samples treated with 2 different methods after 30 days.

treated with the 2% G-CDs solution consistently exhibit a higher relative percentage of oxygen. This relative increase is attributed to the greater concentration of carboxyl (-COOH) and hydroxyl (-OH) functional groups present in the 2% G-CDs solution, which are attached to the carbon dots. Interestingly, the percentage of carbon does not reliably reflect the relative abundance of carbon dots. This discrepancy is likely due to the lower K-α x-ray energy of carbon (0.277 keV) compared to oxygen (0.529 keV), making oxygen more readily detectable by EDS. Furthermore, comparing similar surfaces treated by the 1% and 2% G-CDs solutions, the surfaces treated with the 2% G-CDs solution consistently show a relatively smaller percentage of aluminum than the surfaces treated with the 1% G-CDs solution. This is consistent with the observation that the residual layer left by the 2% G-CDs solution masks certain regions of the aluminum substrate, resulting in less aluminum being detected.

Oxygen is a more reliable indicator of relative changes in the abundance of carbon dots than carbon, as the lower K-α x-ray energy of carbon make it more difficult to detect by EDS than oxygen [27,28]. The 2% G-CDs solution leaves a residual layer that masks the presence of aluminum in the EDS analysis. This is reflected in the dark areas in the maps of aluminum distribution for surfaces treated with the 2% G-CDs solution. This is also reflected in relative reductions in percentage of aluminum reported when comparing similar surfaces treated with the 1% versus 2% G-CDs solution. The dark spots in the distribution maps can also be attributed to large surface features causing shadowing in the EDS results. The shadowing is present on surfaces treated by both Method I and Method II, with the rough surfaces exhibiting peaks and valleys, wherein the x-rays emitted by the valleys are detected less due to shadowing by the peaks. Although masking and shadowing introduce significant errors into the EDS quantitative analysis, the results can still be useful in determining relative differences between similar surfaces.

### *3.3 Surface Wettability*

To investigate the static wetting characteristics of the treated surfaces for both AlSi10Mg and Ti6Al4V 3D printed samples, each sample was positioned horizontally. A 5 µL water droplet was gently deposited onto the surface, and its spreading behavior was recorded using a contact angle goniometer. The initial water contact angle (θw) measurements for the untreated samples, as shown in Fig. 9a, indicate that all as-built surfaces exhibit hydrophilic behavior, with an average θw of approximately 50°. However, after one month of air exposure, θw increases significantly due to a reduction in surface energy. This temporal change is primarily attributed to the absorption of airborne organic contaminants such as long-chain hydrocarbons, carboxylic acids, carbonyl compounds, and diol groups on the surface, which passivate high-energy sites and lower wettability [29]. The instability of surface wettability over time is a well-documented phenomenon in additively manufactured metal parts[8].

Fig. 9b presents the water contact angle measurements for samples treated using Method I and Method II, evaluated after 30 days of environmental exposure. These long-term results highlight the durability of surface modifications. Both AlSi10Mg= and AlSi10Mg// maintained their superhydrophilic properties, exhibiting a contact angle of zero degree in both treatment methods. Similarly, Ti6Al4V= and Ti6Al4V// also demonstrated sustained superhydrophilicity. However, for Ti6Al4V= treated with Method I, a slight increase in contact angle was observed, reaching approximately 8°, indicating a minor reduction in wettability over time. This suggests that while both methods are effective, Method II may offer slightly better long-term stability for Ti-based alloys.

### *3.4 Wicking Dynamics*

To evaluate the surface wetting properties of the AlSi10Mg and Ti6Al4V samples which were fabricated with method II with two different G-CDs concentrations, the spreading behavior of a water droplet on their horizontal surfaces was recorded. As shown in Fig. 10a the specimen was positioned horizontally, and an LED light was used to illuminate the processed surface. A distilled water droplet with 5µL volume was introduced at the middle part of each sample and the progress of water droplet spreading was recorded with a CCD camera. The area (113 $mm^2$) for each sample at different frame was calculated using ImageJ.

As shown in Fig. 10b, the time required for a water droplet to completely spread over the treated surface of AlSi10Mg (=) coated with 1% G-CDs was 1.22 seconds, which decreased slightly to 1.17 seconds when the coating concentration was increased to 2%. At any given moment before reaching the final time, the water droplet area on AlSi10Mg (=) coated with 1% G-CDs is slightly larger compared to that on AlSi10Mg coated with 2% G-CDs. However, the total time to reach the final state is shorter for the sample coated with 2% G-CDs. Similarly, for AlSi10Mg (//), the spreading time decreased from 1.27 seconds with 1% G-CDs coating to 1.19 seconds with 2% G-CDs coating. At any given time, the droplet area was always higher for 2% G-CDs

than 1% G-CDs. This indicates an enhancement in spreading behavior with higher coating concentration.

A comparable trend is observed in Fig. 10c for Ti6Al4V substrates. For Ti6Al4V (=) coated with 1% G-CDs, the droplet required 2.37 seconds to spread across the treated area, whereas the time was reduced to 1.35 seconds with 2% G-CDs. In the case of Ti6Al4V (//), the spreading time decreased from 2.5 seconds (1% G-CDs) to 1.44 seconds (2% G-CDs). These results consistently show that water droplets spread more rapidly on both AlSi10Mg and Ti6Al4V surfaces when coated with 2% G-CDs compared to 1% G-CDs. This improvement in spreading kinetics is attributed to the higher density of functional groups present in the 2% G-CDs coating, which enhances the surface's hydrophilic character and promotes faster droplet spreading.

Furthermore, to assess the wicking behavior of the treated surface, water-spreading dynamics were recorded on a vertically oriented specimen, as shown in Fig. 11a. The samples used in this experiment were fabricated using Method II and coated with 1% G-CDs. A 5 µL droplet of distilled water was dispensed at the base of the laser-fabricated micro-trenches using a micropipette. The spreading motion was captured at 2000 frames per second using an IDT X-StreamVision XS-3 CCD camera. To ensure uniform illumination during recording, LED lights were arranged around the setup.

Upon contacting the textured surface, the droplet initiated a liquid front that moved along the micro-trenches. ImageJ, an open-source image processing software, was employed to track and quantify the wicking distance over time. As shown in fig. 11b, to characterize the fluid transport behavior, the distance of water movement on the vertically oriented surface was plotted as a function of the time$^{0.5}$. This approach allows assessment of the wicking dynamics and is commonly used to evaluate capillary-driven flow. The wicking behavior demonstrated strong anisotropy, with liquid preferentially advancing along the micro-trenches. As shown in Fig. 11c, Initially, the droplet spread laterally, but as sidewise movement diminished, the liquid primarily propagated in the vertical direction. Within 300 milliseconds, for the AlSi10Mg= liquid front ascended nearly 12.5 mm against gravity, achieving an average propagation velocity of approximately 4.1 cm/s, while for the Ti6Al4V= the water droplet moves vertically approximately 11.2 mm with an average speed of 3.7 cm/s. (shown in Fig. 11d).

The capillary effect, commonly observed in tubes, is a well-known phenomenon in fluid dynamics. This

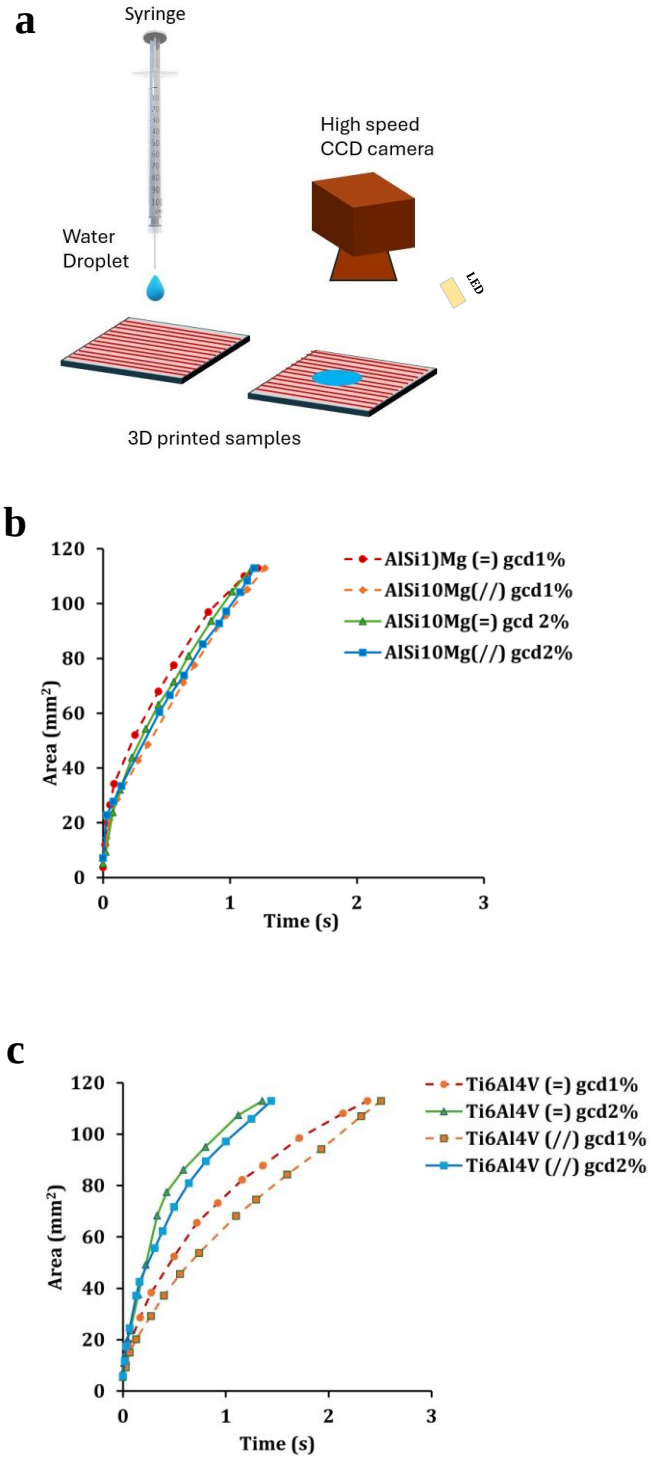


Fig. 10. Measurement of dynamic spreading of water droplet: (a) Schematic of the experimental set up (b) Measurement data for AlSi10Mg surfaces treated with two different G-CDs concentrations (c) Measurement data for Ti6Al4V surfaces treated with two different G-CDs concentrations.

effect is also present in open half-tubes or channels. By creating a series of parallel microgrooves on the surface of a substrate, it is possible to produce a strong capillary surface over a large area. In this work, unidirectional microgrooves were intentionally fabricated to direct the flow of water in a single direction, thereby maximizing the wicking effect along that path. This design allows for the creation of a superwicking surface, where water molecules are rapidly drawn through the micro-trenches due to capillary forces.

However, it is important to note that the capillary force within a half-tube is generally weaker than that in a full tube [30]. The dynamics of liquid movement within a vertical closed tube can be described by the Washburn equation, which models the time-dependent penetration of liquid through porous media [31]. This equation provides a framework for understanding how the liquid spreads and moves within microstructural channels, and it can also be applied to analyze the wicking behavior on surfaces with engineered textures, such as the microgrooves in this study.

$$h\,(t) = \left(\frac{\gamma r cos\theta}{2\mu}\right)^{0.5} * t^{0.5} = (Dt)^{0.5} \qquad (1)$$

where h(t) is the transport distance over time, γ is surface tension, μ is viscosity, r is capillary radius, θ is the contact angle, and D is the capillary performance parameter.

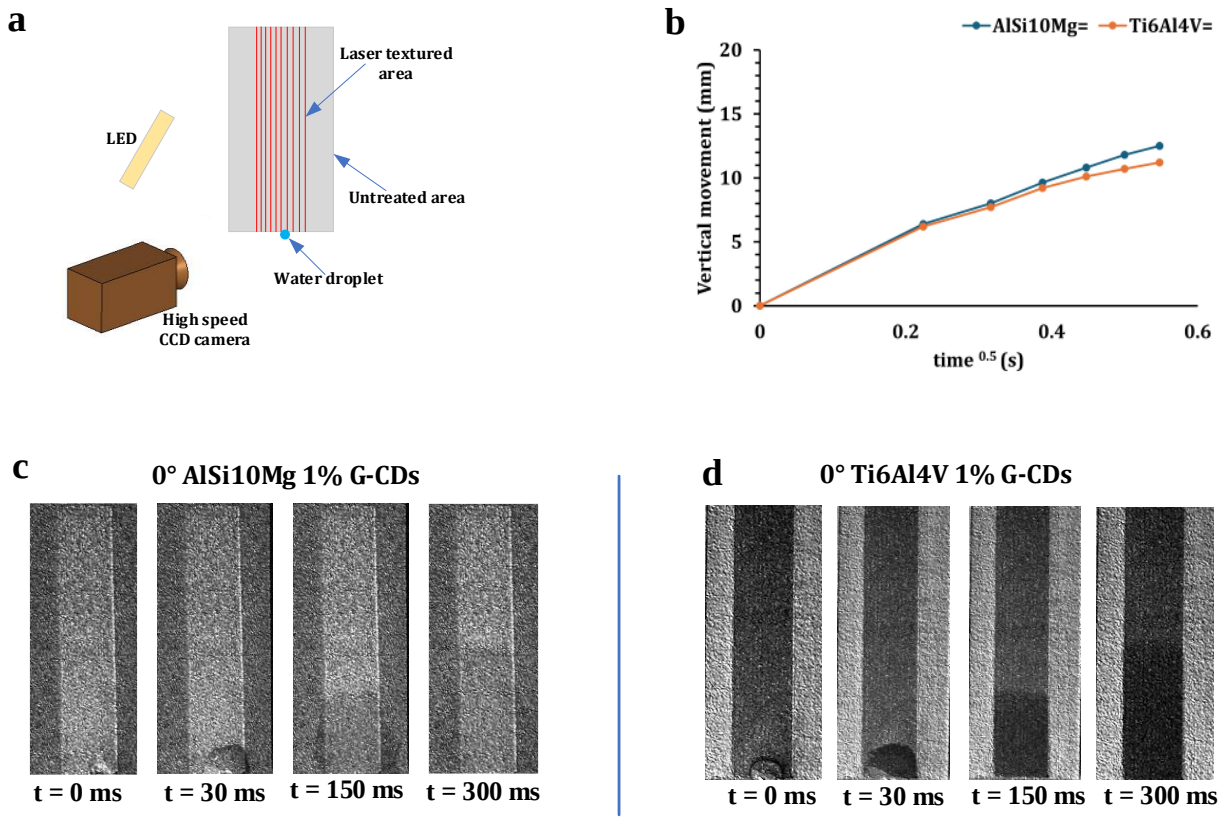


Fig. 11. Variation of dynamic behavior of water droplet (a) schematic of the experimental set up (b) plot of the vertical uphill spreading distance of wetting front against time $^{0.5}$; (c) Sequential progression of water moving uphill for AlSi10Mg (=) sample and (d) Sequential progression of water moving uphill for Ti6Al4V (=) sample.

### *3.4 Thermal Stability of Carbon Dots Coating*

To evaluate the thermal stability of the G-CDs-coated surfaces, samples were exposed to elevated temperatures ranging from 25 °C to 100 °C. In this experiment, the samples were heated in an oven and then allowed to cool naturally to room temperature (25 °C) in ambient air. Subsequently, static water contact angle measurements were performed at room temperature by depositing a 5 µL water droplet on the surface to assess any thermally induced changes in wettability. As illustrated in Fig. 12, at room temperature (25 °C) and 40 °C, all samples exhibited excellent superhydrophilic behavior with a contact angle of zero. However, as the temperature increased, a gradual rise in contact angle was observed, particularly in the samples coated with 1% G-CDs. At 60 °C, both AlSi10Mg (=) and AlSi10Mg (//) samples coated with 1% G-CDs showed an increase in contact angle to approximately 20°. In contrast, the samples coated with 2% G-CDs maintained their superhydrophilic nature at the same temperature, with a contact angle remaining at zero.

At 80 °C, a similar trend was observed; the samples coated with 1% G-CDs exhibited reduced thermal stability, as indicated by an increase in contact angle. This change in wettability at higher temperatures is likely due to the thermal degradation of surface functional groups on the G-CDs. These groups, such as hydroxyl and carboxyl, are essential for maintaining superhydrophilicity. As the temperature increases, these functional groups can oxidize or detach from the carbon dot surface, reducing the material's ability to interact with water. This degradation leads to an increase in contact angle, particularly in samples with lower G-CDs content. In contrast, the samples coated with 2% G-CDs demonstrated better thermal stability, likely due to the higher density of functional groups, which provides more resistance to thermal oxidation and helps maintain surface hydrophilicity. Similar thermal degradation behavior of carbon dots has been reported in the literature, where elevated temperatures caused a decline in surface activity and photoluminescence due to the loss of functional groups [32].

## 4. Conclusions

This study demonstrates two effective and environmentally friendly methods for achieving durable superhydrophilic surfaces on L-PBF-fabricated AlSi10Mg and Ti6Al4V parts. Method I involves coating with gel-like carbon dots (G-CDs), while Method II integrates nanosecond laser texturing followed by G-CDs application. Both methods maintain water contact angles below 10° for over 30 days. The laser-textured surfaces exhibit superwicking behavior, enhancing capillary-driven transport and enabling directional fluid control through engineered microgrooves. Subsequent G-CDs coating further stabilizes the superwicking effect. In addition, Surfaces treated with 2% G-CDs demonstrated faster water spreading and retained superhydrophilicity even at elevated temperatures. These findings highlight the synergistic effects of surface texturing and organic functionalization, offering a promising PFAS-free approach for applications in fluid transport and thermal management.

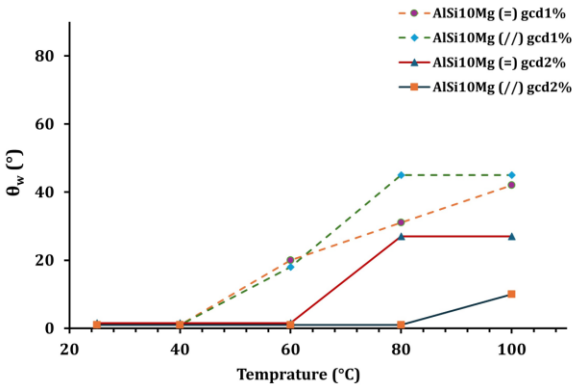


Fig. 12. Contact angle measurements of AlSi10Mg samples with 1% and 2% G-CDs coatings at different temperatures.

It is worth noting that the current method is best suited for accessible external surfaces. Applying it to intricate geometries or internal channels remains challenging due to limitations in laser accessibility and uniform coating coverage. Future work will explore alternative laser delivery systems and coating techniques to address these complexities.


## Acknowledgement

The authors gratefully acknowledge the financial support from the National Science Foundation under Grant Number 2242763. We also appreciate the assistance from Cong Wang's group at the University of Iowa for wetting measurements.

## Contributions

M. Mohammadzadeh conducted experiments, surface and wicking characterizations. B. Nelson prepared the 3D printed samples and surface characterizations Mohammad Ikram Haider helped with the experiments. H. Ding developed the theoretical concepts, experimental approach, and supervised the investigation. M. Mohammadzadeh composed the manuscript. H. Ding revised and finalized the manuscript. All participants discussed the results and commented on the manuscript.

## Declaration of Competing Interest

The authors declare that they have no known competing financial interests or personal relationships that could have appeared to influence the work reported in this paper.

## References


[1] M. Taghian, M.H. Mosallanejad, E. Lannunziata, G. Del Greco, L. Iuliano, A. Saboori, Laser powder bed fusion of metallic components: Latest progress in productivity, quality, and cost perspectives, Journal of Materials Research and Technology 27 (2023) 6484–6500. https://doi.org/10.1016/j.jmrt.2023.11.049.

[2] S. Chowdhury, N. Yadaiah, C. Prakash, S. Ramakrishna, S. Dixit, L.R. Gupta, D. Buddhi, Laser powder bed fusion: a state-of-the-art review of the technology, materials, properties & defects, and numerical modelling, Journal of Materials Research and Technology 20 (2022) 2109–2172. https://doi.org/10.1016/j.jmrt.2022.07.121.

[3] J. Ni, H. Ling, S. Zhang, Z. Wang, Z. Peng, C. Benyshek, R. Zan, A.K. Miri, Z. Li, X. Zhang, J. Lee, K.J. Lee, H.J. Kim, P. Tebon, T. Hoffman, M.R. Dokmeci, N. Ashammakhi, X. Li, A. Khademhosseini, Three-dimensional printing of metals for biomedical applications, Mater. Today Bio 3 (2019). https://doi.org/10.1016/j.mtbio.2019.100024.

[4] Q. Wei, H. Li, G. Liu, Y. He, Y. Wang, Y.E. Tan, D. Wang, X. Peng, G. Yang, N. Tsubaki, Metal 3D printing technology for functional integration of catalytic system, Nat. Commun. 11 (2020) 1–8.

[5] B.W. Reynolds, C.J. Fee, K.R. Morison, D.J. Holland, Characterisation of Heat Transfer within 3D Printed TPMS Heat Exchangers, Int. J. Heat Mass Transf. 212 (2023). https://doi.org/10.1016/j.ijheatmasstransfer.2023.124264.

[6] T. Dixit, E. Al-Hajri, M.C. Paul, P. Nithiarasu, S. Kumar, High performance, microarchitected, compact heat exchanger enabled by 3D printing, Appl. Therm. Eng. 210 (2022). https://doi.org/10.1016/j.applthermaleng.2022.118339.

[7] T. de Rubeis, A. Ciccozzi, L. Giusti, D. Ambrosini, On the use of 3D printing to enhance the thermal performance of building envelope – A review, Journal of Building Engineering 95 (2024). https://doi.org/10.1016/j.jobe.2024.110284.

[8] B. Nelson, W. Huang, N. Shen, S. Shaw, C. Lamuta, H. Ding, Evolving surface wettability in laser-powder bed fusion printed metal parts, Manuf. Lett. 40 (2024) 45–49. https://doi.org/10.1016/j.mfglet.2024.02.003.

[9] W. Huang, B. Nelson, S. Tian, R. Ordikhani-Seyedlar, R.C.Y. Auyeung, A. Samanta, H. Hu, S. Shaw, C. Lamuta, H. Ding, Superhydrophobic surface processing for metal 3D printed parts, Appl. Mater. Today 29 (2022). https://doi.org/10.1016/j.apmt.2022.101630.

[10] Q. Wang, A. Samanta, S.K. Shaw, H. Hu, H. Ding, Nanosecond laser-based high-throughput surface nanostructuring (nHSN), Appl. Surf. Sci. 507 (2020) 145136. https://doi.org/10.1016/j.apsusc.2019.145136.

[11] M. Mohammadzadeh Sanandaji, H. Fu, H. Ding, Slippery liquid-infused porous surfaces on 3D-printed metals, J. Manuf. Process. 167 (2026) 211–220. https://doi.org/10.1016/j.jmapro.2026.03.080.

[12] J. Sun, W. Wang, Z. Liu, B. Li, K. Xing, Z. Yang, Study on selective laser melting 316L stainless steel parts with superhydrophobic surface, Appl. Surf. Sci. 533 (2020). https://doi.org/10.1016/j.apsusc.2020.147445.

[13] J. Neukäufer, B. Seyfang, T. Grützner, Investigation of Contact Angles and Surface

Morphology of 3D-Printed Materials, Ind. Eng. Chem. Res. 59 (2020) 6761–6766. https://doi.org/10.1021/acs.iecr.0c00430.

[14] J. Zhou, X. Han, H. Li, S. Liu, J. Yi, Investigation of layer-by-layer laser remelting to improve surface quality, microstructure, and mechanical properties of laser powder bed fused AlSi10Mg alloy, Mater. Des. 210 (2021). https://doi.org/10.1016/j.matdes.2021.110092.

[15] L. Jiao, Z.Y. Chua, S.K. Moon, J. Song, G. Bi, H. Zheng, Femtosecond laser produced hydrophobic hierarchical structures on additive manufacturing parts, Nanomaterials 8 (2018). https://doi.org/10.3390/nano8080601.

[16] D.P. Zhao, J.C. Tang, H.M. Nie, Y. Zhang, Y.K. Chen, X. Zhang, H.X. Li, M. Yan, Macro-micron-nano-featured surface topography of Ti-6Al-4V alloy for biomedical applications, Rare Metals 37 (2018) 1055–1063. https://doi.org/10.1007/s12598-018-1150-7.

[17] T. Thenard, A. Catapano, R. Allena, M. Mesnard, N. Saintier, E.M. Mohamed, T. Thenard, A. Catapano, R. Allena, M. El May, N. Saintier, M. Mesnard, Topography and wettability characterization of surfaces manufactured by SLM and treated by chemical etching, Mechanics of Advanced Materials and Structures (2020) 1–18. https://doi.org/10.1080/15376494.2020.1836292ï.

[18] O. Keles, A. Qadeer, B.S. Yilbas, Wetting state of 3D printed Ti-6Al-4V alloy surface, Advances in Materials and Processing Technologies 8 (2022) 2465–2475. https://doi.org/10.1080/2374068X.2021.1912539.

[19] M. Mohammadzadeh Sanandaji, R. Mollick, A. Ratner, H. Ding, Laser-enabled organic coating for sustainable PFAS-free metal surfaces, Manuf. Lett. 45 (2025) 8–12. https://doi.org/10.1016/j.mfglet.2025.06.198.

[20] M. Mohammadzadeh, R. Mollick, A. Ratner, H. Ding, Laser-enabled organic coating for sustainable PFAS-free metal surfaces, Manuf. Lett. (2025). https://doi.org/10.1016/j.mfglet.2025.06.198.

[21] Y. Zhou, A.E. ElMetwally, J. Chen, W. Shi, E.K. Cilingir, B. Walters, K.J. Mintz, C. Martin, B.C.L.B. Ferreira, W. Zhang, S.D. Hettiarachchi, L.F. Serafim, P.L. Blackwelder, A.H. Wikramanayake, Z. Peng, R.M. Leblanc, Gel-like carbon dots: A high-performance future photocatalyst, J. Colloid Interface Sci. 599 (2021) 519–532. https://doi.org/10.1016/J.JCIS.2021.04.121.

[22] J. Zuo, T. Jiang, X. Zhao, X. Xiong, S. Xiao, Z. Zhu, Preparation and Application of Fluorescent Carbon Dots, J. Nanomater. 2015 (2015). https://doi.org/10.1155/2015/787862.

[23] R. Mollick, N. Hentges, S. Parveg, Y. Zhou, R.M. Leblanc, A. Ratner, Proceedings of the ASME 2022 International Mechanical Engineering Congress and Exposition IMECE2022, n.d.

[24] A.B. Spierings, N. Herres, G. Levy, Influence of the particle size distribution on surface quality and mechanical properties in AM steel parts, Rapid Prototyp. J. 17 (2011) 195–202. https://doi.org/10.1108/13552541111124770.

[25] H. Gong, K. Rafi, H. Gu, T. Starr, B. Stucker, Analysis of defect generation in Ti-6Al-4V parts made using powder bed fusion additive manufacturing processes, Addit. Manuf. 1 (2014) 87–98. https://doi.org/10.1016/j.addma.2014.08.002.

[26] B. Bhushan, Y.C. Jung, Natural and biomimetic artificial surfaces for superhydrophobicity, self-cleaning, low adhesion, and drag reduction, Prog. Mater. Sci. 56 (2011) 1–108. https://doi.org/10.1016/j.pmatsci.2010.04.003.

[27] P. Hovington, V. Timoshevskii, S. Bessette, S. Burgess, P. Statham, H. Demers, R. Gauvin, K. Zaghib, On the Detection Limits of Li K X-rays Using Windowless Energy Dispersive Spectrometer (EDS), Microscopy and Microanalysis 23 (2017) 2024–2025. https://doi.org/10.1017/s1431927617010789.

[28] T. Salge, M. Falke, D. Goran, J. Berlin, T. Salge, M. Falke, D. Goran, Revolutionizing the Chemical Analysis of Chondritic Meteorites at the Micro and Nanometer Scale Article, 2011. https://www.researchgate.net/publication/252138668.

[29] L. Gao, T.J. McCarthy, Contact angle hysteresis explained, Langmuir 22 (2006) 6234–6237. https://doi.org/10.1021/la060254j.

[30] M. Stange, M.E. Dreyer, H.J. Rath, Capillary driven flow in circular cylindrical tubes, Physics of Fluids 15 (2003) 2587–2601. https://doi.org/10.1063/1.1596913.

[31] L.R. Fisher, P.D. Lark, An experimental study of the washburn equation for liquid flow in very fine capillaries, J. Colloid Interface Sci. 69 (1979) 486–492. https://doi.org/10.1016/0021-9797(79)90138-3.

[32] S. Dua, P. Kumar, B. Pani, A. Kaur, M. Khanna, G. Bhatt, Stability of carbon quantum dots: a critical review, RSC Adv. 13 (2023) 13845–13861. https://doi.org/10.1039/d2ra07180k.